processes

MDPI

Communication

Synthetic-Gas Production through Chemical Looping Process with Concentrating Solar Dish: Temperature-Distribution Evaluation

Edoardo Montà [1], Massimo Santarelli [1] and Davide Papurello [1,2,*]

[1] Department of Energy (DENERG), Politecnico di Torino, Corso Duca degli Abruzzi, 24, 10129 Turin, Italy
[2] Energy Center, Politecnico di Torino, Via Borsellino, 38, 10129 Turin, Italy
* Correspondence: davide.papurello@polito.it; Tel.: +39-011-090-8505

Abstract: The energy crisis and the adaptation of the global energy structure promote the development of renewable energies, in particular solar energy, also for syngas production. In this work, attention was focused on solar devices, necessary to provide high-temperature heat for the reduction reaction of metal oxides involved in the chemical looping driven by solar energy. Thermochemical processes for synthetic-gas production and CO_2 sequestration were investigated using a concentrating solar thermal system. This paper proposes a useful forecasting model of the receiver temperature to make a realistic estimate of the system's producibility for the different periods of the year. The model proposed was validated in the winter season, and the predicted temperature varied below 5% considering the real experimental data (442–472 °C). The validated model was used to evaluate the temperature receiver in spring and in summer, when the thermal level is reliable for thermochemical processes. From the spring season until the completion of the summer season, optimum conditions inside the receiver were reached (above 1000 °C). These preliminary findings could be used for the development of large-scale production systems.

Keywords: solar fuels; thermochemical cycles; carbon-dioxide splitting; solar reactors; concentrated solar energy

Citation: Montà, E.; Santarelli, M.; Papurello, D. Synthetic-Gas Production through Chemical Looping Process with Concentrating Solar Dish: Temperature-Distribution Evaluation. *Processes* **2022**, *10*, 1698. https://doi.org/10.3390/pr10091698

Academic Editor: Alfredo Iranzo

Received: 28 July 2022
Accepted: 22 August 2022
Published: 26 August 2022

1. Introduction

Conventional fuels have enabled the development achieved in our society. However, their continued use is a problem for our future development. In this transition phase, it would be unfair to abandon the advantages achieved using fossil fuels. One of the main advantages is the exploitation of existing infrastructure. These infrastructures guarantee the global distribution of fuels. For these reasons, the direct use of synthetic fuels of "non-fossil" origin is an attractive and feasible alternative in the transition phase to totally green fuels. Currently, the term "synthetic fuel (synfuel)" refers to a liquid or gaseous fuel produced on a commercial scale from low-heating-value carbonaceous sources, such as coal, natural gas and other biomass, which are enhanced at the expense of additional energy [1]. Currently, the main production processes still involve fossil fuels. In the Gas-To-Liquid (GTL) process, methane-rich gases are converted into synthetic liquid fuels either via the direct conversion of methane into methanol in one step or using syngas as an intermediate [2–4]. Exothermic conversion processes, mainly the Fischer–Tropsch process, for hydrocarbon production are growing in terms of importance and have been commercially exploited for a long time [2,5,6].

Syngas production using thermochemical processes could be more sustainable when combined with a renewable energy source, such as solar energy, instead of being driven by fossil fuels [7–9]. Three methods for syngas production using solar energy can be found in the literature [1]: photochemical/photobiological, thermochemical and electrochemical methods [10–12]. The photochemical procedure is carried out at a low temperature and

directly uses the energy contained in photons [13,14]. The thermochemical path uses the high-temperature solar heat provided by concentrating systems (CSs) to perform multiple thermochemical reactions able to directly produce syngas from the transformation of fossil and non-fossil fuels [15–17]. Among the various thermochemical cycles, chemical looping, tested in combination with CSs, is directly adapted to the combined splitting of CO_2/H_2O to produce syngas [1]. The electrochemical synthesis method can be used as an alternative to photovoltaics to provide electricity for the high-temperature electrolysis process of steam or vapor/CO_2 mixtures [18,19]. Current research studies are involved in the building of industrial-size plants where solar dishes (>400 kWth) feed the reforming reactor for synthetic-gas production [9]. The main gap is related to the lack of funding to reduce syngas production costs compared with fossil-fuel systems. Other research topics include the geometry of the solar disc [20–23], the heat-transfer medium (solid particles, molten salts, sodium vapors, air, etc.) [24–26] and the receiver material [21,22,27–29], in addition to the development of structured systems with improved thermal performance, such as the use of fins, etc. [30–33]. The other two methods, the photochemical and electrochemical methods, require investment to demonstrate feasibility on large-scale plants. The production costs of these synthetic gases are even higher than those for the thermochemical method. Fang et al. showed how a CP-PV system can be exploited using highly energetic photons [14]. In future studies, they suggested to carry out a tradeoff between PV efficiency (values still low) and electrical efficiency [14]. In a revision work proposed by Yaashikaa et al., detailed reports on photochemical and electrochemical CO_2 transformation were highlighted, and the advantages and disadvantages of the methods proposed were also highlighted [34]. The catalytic aspects are stringent, and research is focused on cost abatement with the increase in the efficiency of conversion. Current limitations of low- and high-temperature electrochemical processes were investigated in the work proposed by Severin et al. [35]. The most significant limitations were those associated with degradation phenomena that occur during operation under realistic conditions, i.e., in transient mode or with the use of processes containing trace contaminants. Advances in the fundamental understanding of degradation mechanisms and the development of stable, high-performance materials are essential for the advancement of this technology. Another study proposed by Hernandez et al. [36] emphasized the fundamental thermodynamic, kinetic and mass-transport aspects required to ensure the good production of CO- and H_2-rich syngas. A competitive approach between the electrochemical reduction of CO_2 and the combination with H_2 was shown. The points highlighted for future development were energy yields and catalytic performance under real conditions. Experimental results in pilot plants showed that conversion yields were higher when considering the thermochemical process rather than the other proposed methods, although scientific research is still needed. A more realistic approach was reported for the thermochemical process using non-stoichiometric cerium oxide. This chemical compound has established itself as a reference redox material for the realization of two-step thermochemical cycles and the generation of sustainable fuels, such as a gas mixture of CO and H_2 [12,15,16,37–39]. The energy sources used to produce syngas play a fundamental role. The thermochemical splitting of CO_2 and H_2O takes advantage of the entire spectrum of solar radiation to produce CO and H_2 [27,40–42], even if the temperature level and thermal energy requirements are fundamental. These aspects, especially in real case studies, which are far from the ideal conditions of the laboratory, require strong research work.

The purpose of the experimental campaign carried out at Energy Center Lab at Polito is to evaluate the feasibility of a chemical looping process with the consequent production of synthetic gas using a concentrating solar thermal dish. In this paper, the calculation of the temperature in the receiver, placed in the focal plane of the parabolic dish, was accomplished. The approach was used to cover the main heat-transfer processes to evaluate the thermal losses. Conductive, convective and radiation losses were considered. These preliminary results were used for the material selection and the technical feasibility of the reduction reaction in a real solar dish concentrator for syngas production.

2. Material and Methods

2.1. Modeling Tools and Mathematical Description of the System

A parabolic mirror focuses the incident solar radiation onto a receiver, thus generating a very high local heat flux, usually exploited to produce steam, which acts as a working heat-transfer fluid in a turbine linked to a generator. In some applications, solar heat can be an excellent alternative to produce syngas through the solar thermal gasification of chemical compounds under supercritical conditions. The synthetic gas produced can be directly used as a fuel source. As mentioned above, the idea behind a parabolic dish is to concentrate the reflected solar radiation, see Figure 1. The rays converge towards an extremely small area onto the focal plane, where a receiver of a different shape is placed according to the needs (Figure 2). The flux uniformity on the receiver surface has a significant impact on both the success and efficiency of the thermochemical reactions to produce syngas. For this reason, as detailed in the following sections, the three-dimensional modeling of the parabolic collector and the receiver were developed, so that the surface distributions of thermal power and temperature in the focal plane could be derived. Numerical modeling was carried out with Comsol Multiphysics, software based on BEM-FEM hybrid technology that allows one to operate with the finite element method, discretizing the continuum with a set of finite-sized partitions, interconnected with each other at predefined points (nodes).

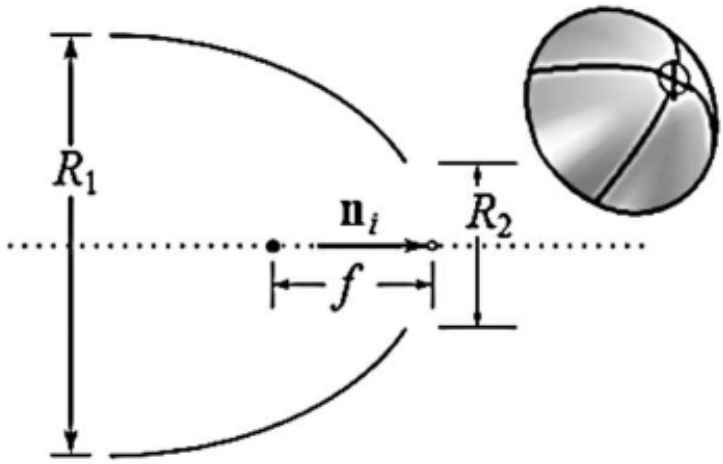

Figure 1. Shell 3D: thin-layer parabolic mirror.

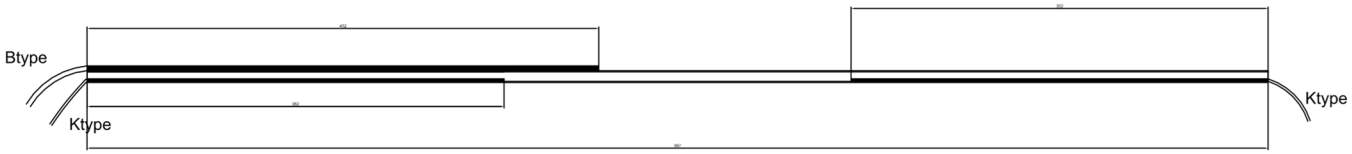

Figure 2. Overall dimensioned view of receiver with thermocouples.

The simulation tool adopted to analyze the system from an optical point of view was the Ray Optics Module, which provides specific modeling instruments for the propagation of electromagnetic waves with an optical geometry technique (ray tracing) based on the rays tracked after the interaction with the surfaces and on the consequent evaluation of the path followed by light. The probabilistic approach adopted for the simulation was based on the Monte Carlo method, since as detailed below, the generation of sun rays purely occurs in an aleatoric manner, and the physical perturbations due to the surface roughness of the mirror and the darkening phenomenon at the edge of the solar disk are randomly sampled from probability distribution functions [43]. The propagated waves are treated as rays that can be reflected, refracted or absorbed into the geometric contours of the model. Although introducing approximations, since the geometry is large with respect

to the wavelength of electromagnetic radiation, the optical beam module is the ideal tool for the realistic visualization of the reflected-ray trajectory.

2.2. Experimental Description

The solar paraboloid used for research was built knowing the focal length and using the section incorporated in the Comsol library relating to the Ray Optics Module. Once the focal length was known, other important parameters that were to be subsequently used in the modeling could be derived. The real temperature data were obtained using a solar concentrator (Elma.net srl, Riva del Garda (TN), Italy) [44] installed on the roof of the Energy Center (Turin, Italy). A graph describing the geometry of the model adopted to create the parabolic reflector is shown below. The simplified structure was characterized by a negligible thickness, while the diameter was calculated according to the geometric parameters (focal length and rim angle):

$$D_{dish} = 4 \cdot f \cdot (\csc(\psi) - \cot(\psi)) \quad (1)$$

The geometry also included a horizontal cylindrical receiver (sintered Alumina 99.7%; Almath crucibles, Newmarket, UK), with the focal plane being in the central section. A dimensioned drawing of the receiver with the corresponding lateral thermocouples is represented below (Figure 3), including a B-type thermocouple (0.5 mm; Tersid, Milan, Italy) with a ceramic sheathing of 8 mm. This thermocouple was in the middle of the receiver, while two K-type thermocouples were at the tube ends (3 mm diameter; Tersid, Milan, Italy) (A1 near the reactor on the left, A3 on the right).

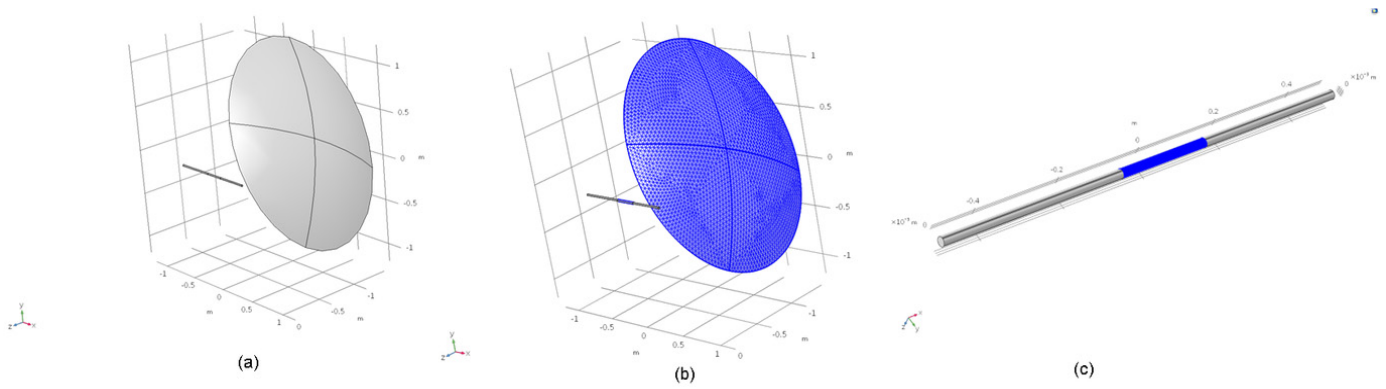

Figure 3. (**a**) Geometrical modeling of the system consisting of solar dish and horizontal cylindrical receiver. (**b**) Mesh created for the reflective surface of the parabolic mirror. (**c**) Geometrical modeling of receiver with the corresponding mesh of the focal plane in the central section.

By entering the appropriate dimensions in the software used, the complete geometric model of the system (dish and receiver) was created (see Figure 4). The entire domain was uniformly discretized into infinitesimal-dimensioned elements to generate an extremely dense mesh to calculate the distributions of the main parameters on the reflective surfaces of the paraboloid and the absorbing ones of the receiver.

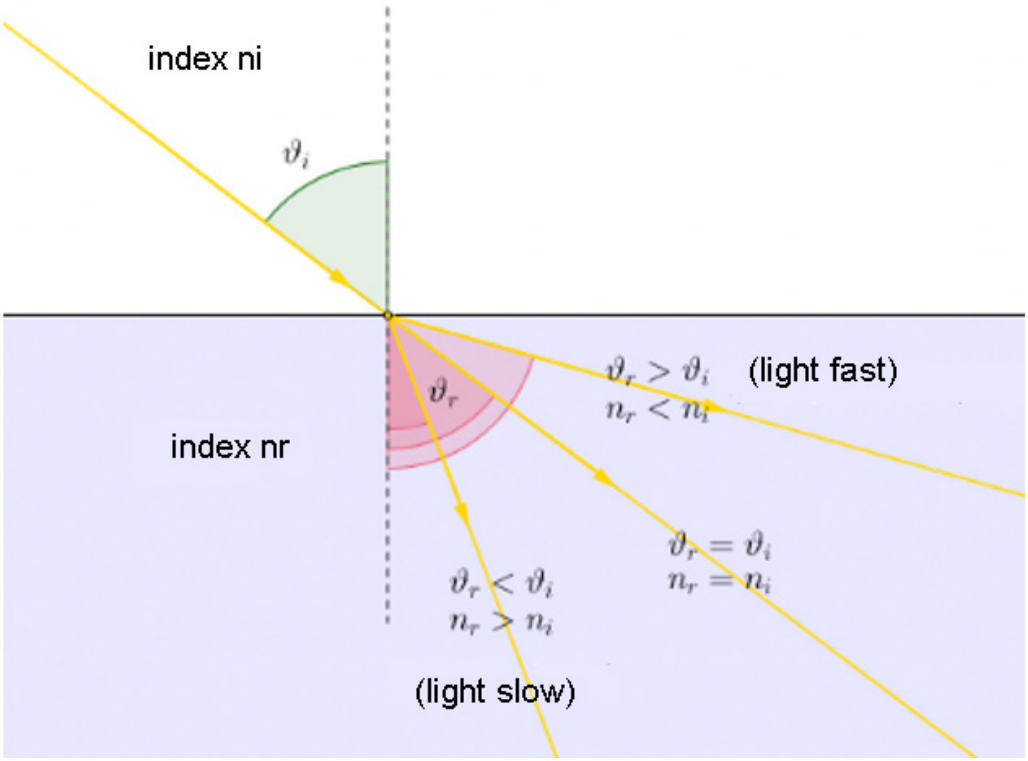

Figure 4. Effect of the phenomenon of refraction of solar radiation [45].

3. Results and Discussions

In this study, the main goal was to forecast the temperature trend of the focal point inside and outside the receiver placed in a solar dish concentrator. The approach used had to consider the main heat-transfer processes; conductive, convective and radiation losses were considered.

3.1. Monte Carlo Ray-Tracing Simulation

Geometric optics is the foundation behind the design of an optical system. Solar radiation can be subject to two different phenomena:

- Refraction: When radiation is refracted, to understand its behavior, it is necessary to refer to Snell's law [45] (see Figure 4). It is possible to distinguish the angle of incidence and the angle of refraction. The possible behaviors are also reported when the refraction angle changes:

$$n_1 \cdot \text{sen}\ \theta_1 = n_2 \cdot \text{sen}\ \theta_2 \rightarrow \frac{n_1}{n_2} = \frac{\text{sen}\ \theta_2}{\text{sen}\ \theta_1} \quad (2)$$

- Reflection: When radiation is reflected by a smooth surface, it obeys the reflection law, according to which the incident and reflected rays form identical angles with respect to the normal to the surface (Figure 5). An important part of the design and analysis steps of solar concentrators concerns ray tracing, which deals with the study of the paths followed by solar rays in systems with reflective and refractive surfaces. For the study of reflected or refracted radiation, it is necessary to follow the procedure shown below.

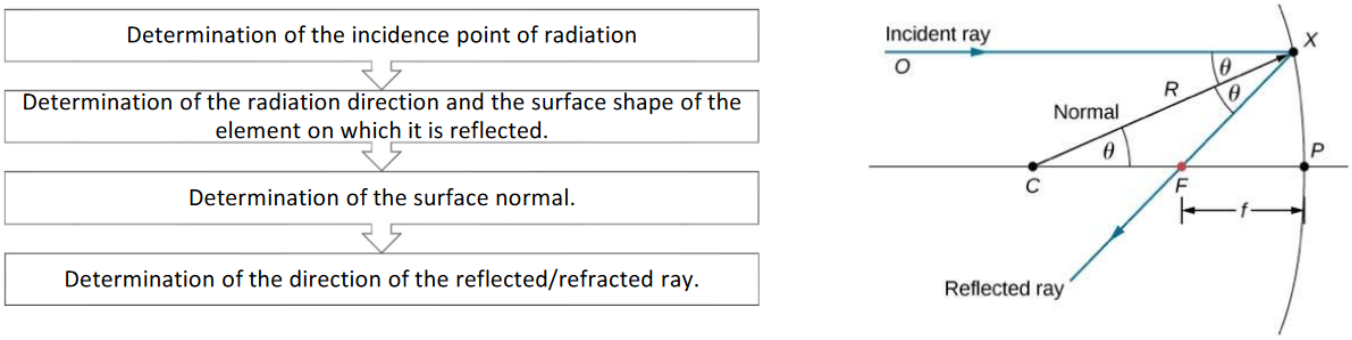

Figure 5. Tracing of direction of rays reflected by a reflective surface.

To quantify the thermal flux distribution in the focal plane of the Energy Center's concentration system, it was necessary to adopt a numerical calculation strategy. Thanks to the Ray Optics Module, a possible evaluation of the solar radiation directly reflected from the parabola surface could be obtained using the "Illuminated Surface" function. The intensity of the reflected radiation strongly depended on the curvature of the paraboloid and thus on the specific trajectory assumed by the beam rays. The direction followed by the released rays depended on the path of the incoming beam vector and the surface normal. A fixed power (intensity of the incident ray) was also assigned to each beam released, the value of which depended on the total power of the source set for the illuminated wall function. When the rays reached the focal plane surface, they were stopped by the "Wall" function, whose function was to simulate the absorptive behavior of the receiver surface (see Figure 6). Here, the ray trajectories were described in terms of power from the dish to the receiver. Figure 6 shows that the maximum power hitting the receiver came from the central part of the dish.

Theoretically, an ideal parabolic reflector could concentrate the rays in one point. However, many perturbations prevent this idealized behavior from happening, even in the context of geometric optics in which diffraction is neglected. Concerning a parabolic reflector, among the several reasons for the system to have a limited focusing capacity, the following phenomena occur:

- Absorption: A significant fraction of the incident radiation is absorbed by the mirrors in a newly installed dish as well as in a parabola whose performance has degraded over time. This means the efficiency tends to decrease;
- Surface roughness: In a real parabolic mirror characterized by a non-perfectly smooth surface, there is always a deviation of the reflected rays different from the ideal case that refers to the surface's normal direction. This causes solar radiation to be imperfectly concentrated, spreading the flux over a wider region of the focal plane;
- Sun's shape: The term refers to the effects of the finite dimensions of the solar disk. If the Sun were an extremely small radiation source, all incident solar rays would be almost parallel. However, this is not the case. Even at a distance of about 150 million kilometers, the Sun is still large enough to allow rays from different parts of the solar disk to create significant angles. The correction included due to the finite size of the Sun implies that incident rays on Earth are sampled to form a very narrow cone (Figure 7) with an opening half-angle equal to θ_s = 4.65 mrad [43].

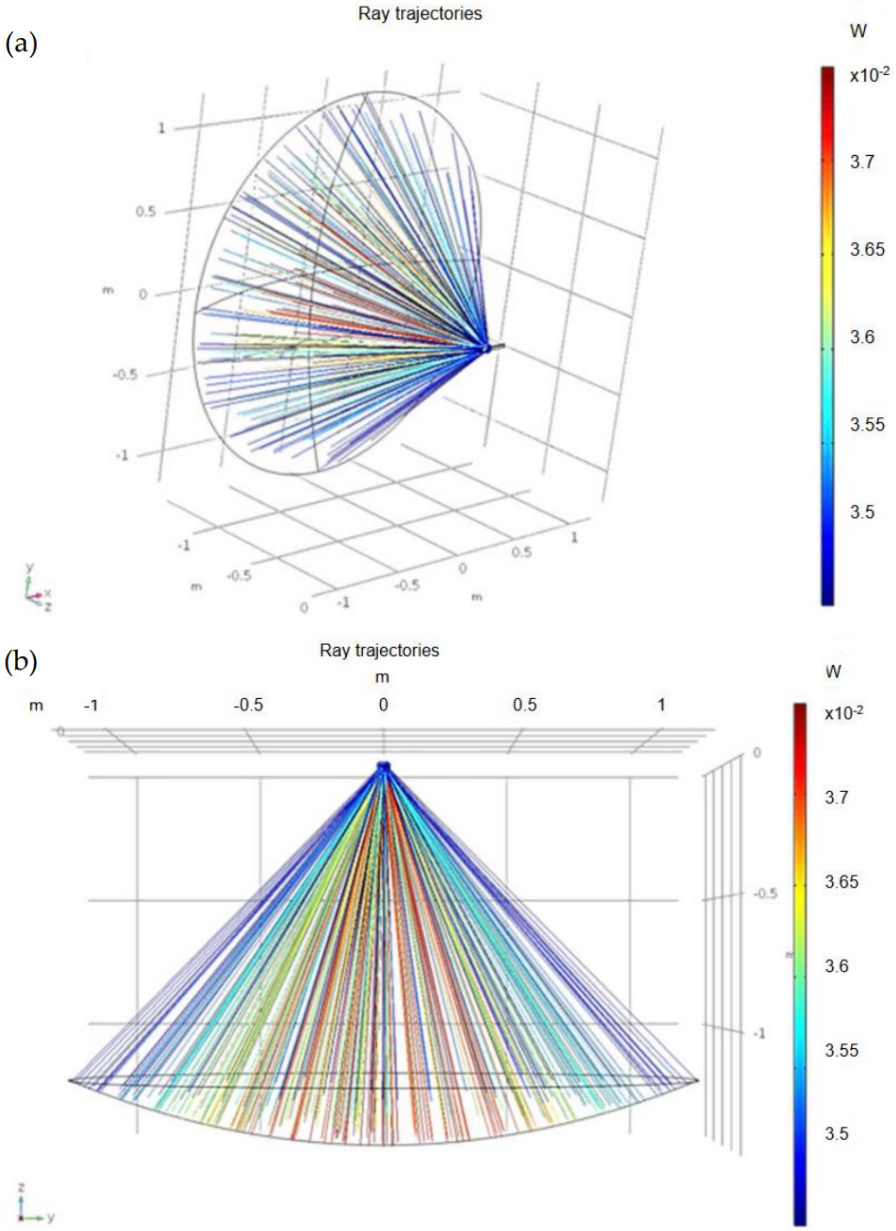

Figure 6. (**a**) Profile view of trajectories of reflected rays. (**b**) Trajectories of reflected rays in terms of deposited power.

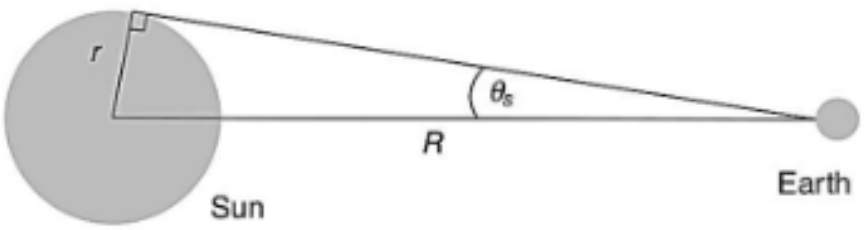

Figure 7. Sampling cone of the rays coming from the solar disk.

Radiation is also emitted from the circumsolar region, i.e., the luminous area surrounding the solar disk, but in the present model, the circumsolar radiation was neglected, assuming CSR = 0.

In addition to influencing the spatial and directional distribution of the rays, another aspect related to the Sun's shape is the relative intensity of radiation coming from different

parts of the solar disk. Radiation from the center of the solar disk is generally brighter than that emitted from outside the disk. This phenomenon, also known as limb darkening, is responsible for the decrease in light intensity coming from the Sun near the perimeter of the visible disc [44].

Among the various computational models available to simulate the propagation of reflected rays, ray tracking using the Monte Carlo method allows one to take into consideration the diameter of the finished source, limb darkening, surface roughness and the absorption of the mirror. The model proposed was based on two studies, each of which corresponded to a different characterization of the "Illuminated surface" function. For each study, sampled rays were released from 100,000 distinct points. At each point, the direction of the incident ray was then changed by a random angle; the probability density of these angular variations was uniform within a cone of angle ψ_s.

For the first study, no limb-darkening model was used, and the surface was assumed to be perfectly smooth and reflective (the absorption coefficient was set to 0, which meant that 100% of the incoming radiation was reflected). The rays sampled were under the conical distribution, and they considered the maximum opening angle of the solar disk θ_s. The intensity considered for the incident rays was equal to 800 W/m^2, while the total power of the source was determined as $P_{source} = A_0\ I_{0.}$

The implementation of a simplified model is useful to have as a reference of the most idealistic solution, in which the finite dimensions of the Sun are considered, but all other factors are neglected. If the paraboloid were a smooth reflector and the sun's rays propagated as plane wavefronts emitted by an infinitely distant point source, then all the incoming radiation would be focused in a very limited area of the collector, located right in the center of the paraboloid (Figure 8). The ideal focusing system would consist of a flawless dish able to concentrate the collimated solar radiation into an infinitely small point on the focal plane. Figure 9 shows the spatial distribution of the deposited power of the rays intercepted by the reflecting surface of an ideal reflector. A well-defined power value I_{th} was assigned to each beam released; therefore, the innermost area was the one on which most of the rays collided, depositing the highest power contribution. It was observed that the more the radial distance decreased, the more the density of the incident radiation, and consequently the absorbed power, increased.

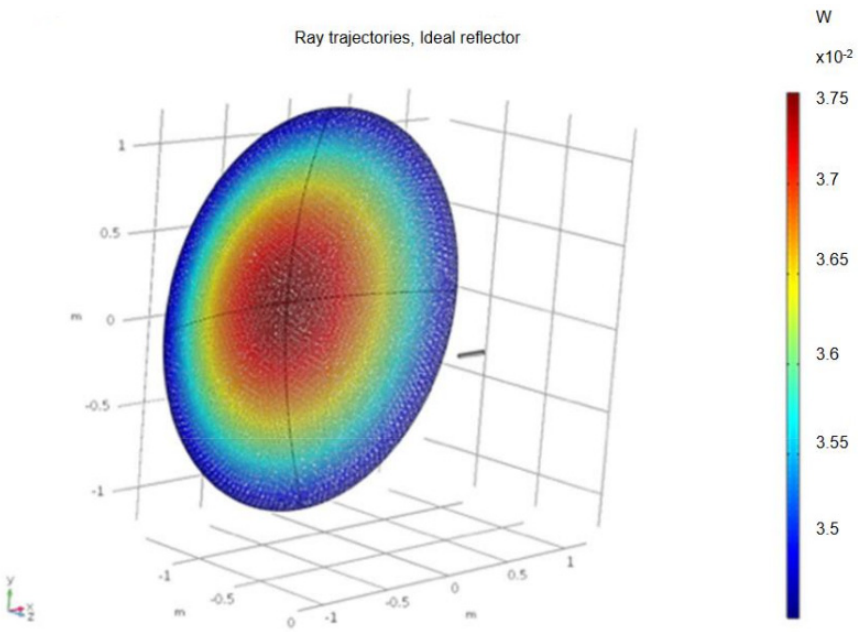

Figure 8. Distribution of incident rays on ideal reflector. The chromaticity of each point indicates the power value deposited.

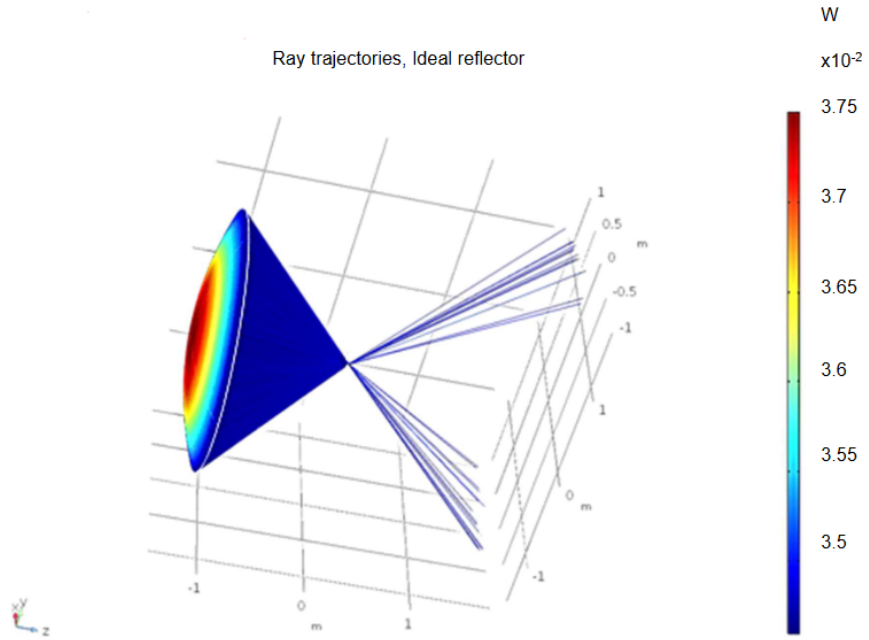

Figure 9. Trajectories of rays reflected by ideal reflector and focused onto receiver in terms of power density.

The peripheral areas of the paraboloid, while contributing to the reflection of rays, were those that focus radiation to a lesser extent on the focal plane. In the ideal model, there was considerable precision in the reflection of rays by the reflector; therefore, the concentration of radiation was the best possible, i.e., the dispersion of rays reaching the focal plane and not perfectly absorbed was limited. It could be observed that the two beams in Figure 9, due to the non-perfect incidence in the center of the receiver, tended to reflect again on the circular walls of the horizontal cylinder. Almost every beam was stopped by the receiver, with only an extremely small number of beams visibly propagating beyond the focal plane.

The reflection coefficient, as in the ideal case, was set based on the absorption coefficient of the mirror, which in this case corresponded to the value declared by the manufacturer of the solar disk [44], i.e., $\alpha = 0.2$; therefore, 80% of the radiation was reflected. The ray sampling remained unchanged, following the conical distribution, as did the intensity of incident rays, equal to 800 W/m^2, and the total power of the source, $P_{source} = A_0 I_0$. The spatial distribution of the rays captured by the surface of a reflector in the real case, in terms of power deposited, was much more heterogeneous (Figure 10) as a consequence of the darkening phenomenon at the edge of the solar disk. The rays affected the entire surface of the paraboloid in a purely random way, without defining an area characterized by greater power density. The central and peripheral areas of the paraboloid, which contributed to the reflection of rays in the same way, focused the radiation on the focal plane. The ray trajectories resulting from the second study are shown in Figure 11. Compared with Figure 9, a considerable number of beams did not perfectly affect the target and continued to propagate, reducing the efficiency of the receiver. These results were comparable with those achieved by Lee, in whose paper, the surface slope error was investigated in detail [46], and the limb-darkening attenuation for the energy distribution of the solar disk was evaluated according to Buie et al. [47].

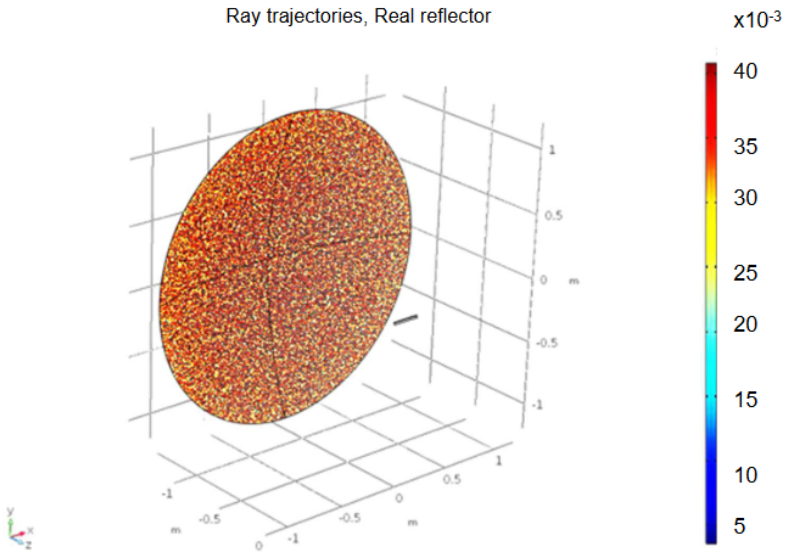

Figure 10. Since the surface of the disc was not perfectly smooth, the reflected rays were not all released in the exact theoretical direction but underwent completely random deviations.

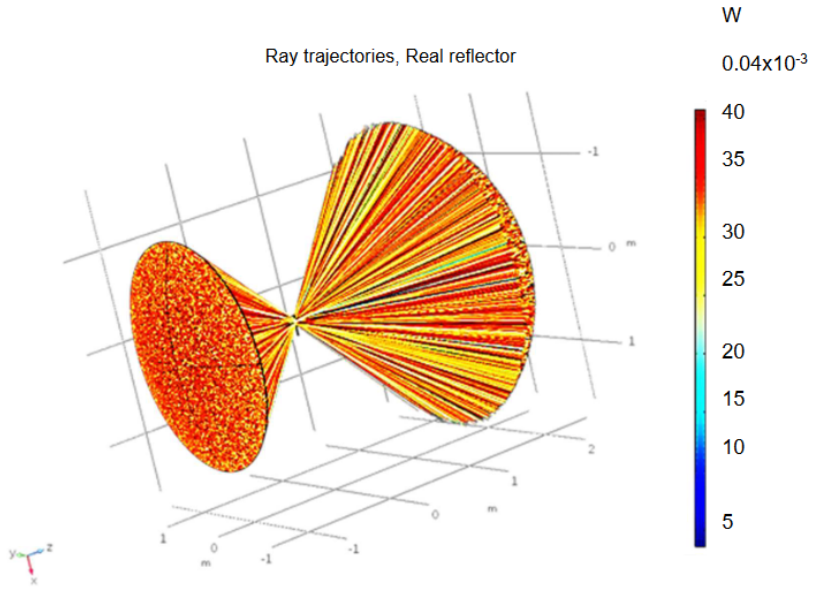

Figure 11. Trajectories of rays reflected by a real reflector and focused onto the receiver. Surface roughness, solar limb darkening and absorption were considered.

3.2. FEM Simulation Results with Ideal Solar Irradiance

To clarify the logical flow followed to create the numerical modeling of the concentrator/receiver system in Comsol Multiphysics, a summary list of the main instructions is provided in the table below.

The main operating parameters concerning the heated surface placed in the focal area of the concentrator were evaluated based on the ideal condition of solar irradiance, I_0, following the maximum radiative flux reported on the paraboloid user manual [44] and concerning the geometry of the system. The solar rays reaching the surface of the focal plane were stopped by the "Wall" function, so that an estimate of the thermal flux deposited could be carried out using the "Deposited Ray Power" function. Ansys, Comsol and other software can be used for numerical investigation purposes [48–50].

Since solar energy was collected in a large area, much larger than the receiving surface of the focal plane, the thermal power deposited was extremely high. The central section of the horizontal cylindrical receiver used in this research study had the purpose to accumulate

the heat necessary to reach the thermal conditions so that the thermochemical reactions of interest could take place. In this regard, a comparative analysis between the temperatures and the deposited powers in the focal plane of the receiver was carried out both for the surface hit by the rays reflected by the idealized concentrator (Figure 9) and the real concentrator (Figure 11). It was interesting to notice that for the ideal case (Figure 12), a very high deposited thermal flux was observed, with a maximum value of approximately 2.41 10^7 W/m^2 near the center of the focal plane. Bekele et al. used a similar thermal flux deposited in the receiver [22].

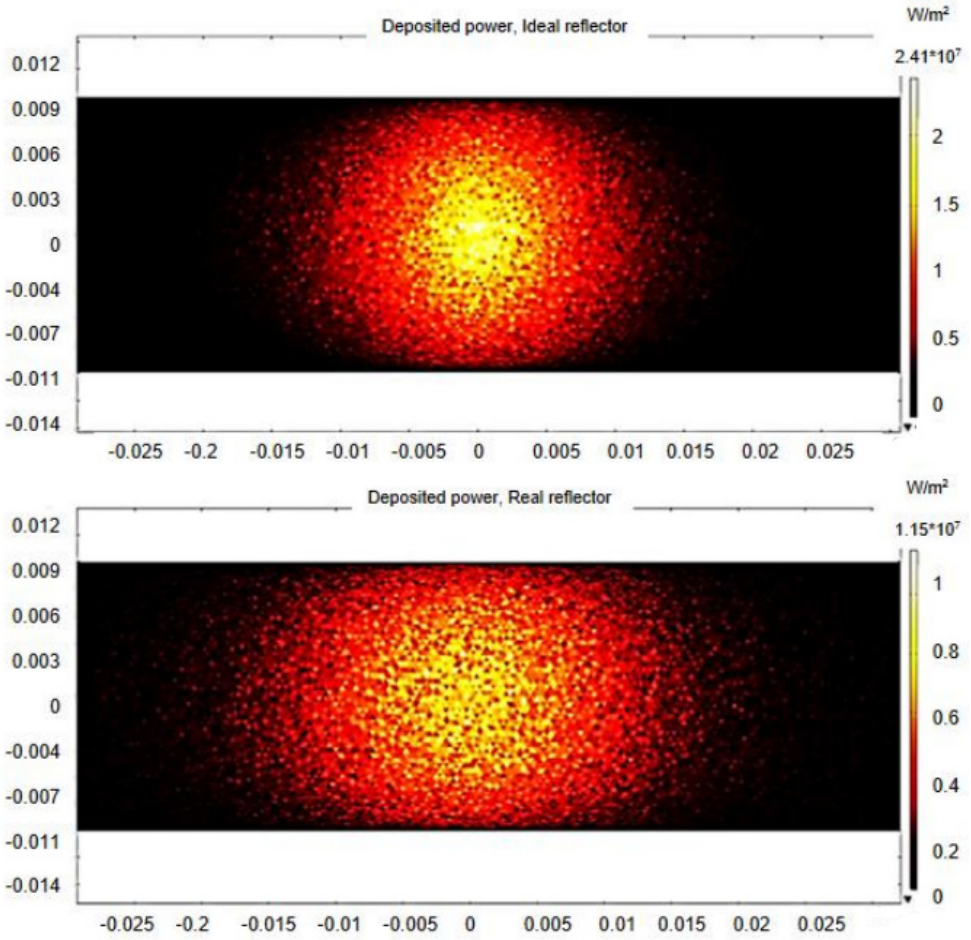

Figure 12. Distribution of thermal power deposited in the focal plane of receiver. Ideal case (**above**): perfectly smooth and reflective parabolic reflector; the phenomenon of solar limb darkening was neglected. Real case (**below**): parabolic reflector in which factors such as surface roughness, absorption and solar limb darkening were included.

The distribution was also somewhat homogeneous and approximately circular in shape. A different situation occurred for the real case (Figure 12); the greater dispersion of the rays reflected by the non-idealized concentrator caused an enlargement in the concentration surface, this time characterized by an elliptical shape. This further led to a lower concentration of the thermal flow, which reached a maximum value of 1.15 $\times$ 10^7 W/m^2. Similar to surface roughness, the effect of the Sun's shape tended to spread the heat flow over a larger region of the focal plane. Similar approach and results were achieved by Lee et al. [46]. Furthermore, when rays were released from points outside the center of the solar disk, their initial intensity was reduced as a direct effect of the solar-edge-darkening phenomenon (limb darkening), as supported by Buie et al. [47]. The real incident flux in the three-dimensional focal plane, as shown in Figure 13, showed how the distribution was much more extended and covered a larger surface than the ideal case. The explanation is

given by the fact that the concentration of rays was not characterized by the same precision because of all those phenomena that prevent a real system from functioning as a flawless disk. The maximum flow was also considerably reduced, reaching a peak value of less than half of that of the ideal case (Table 1).

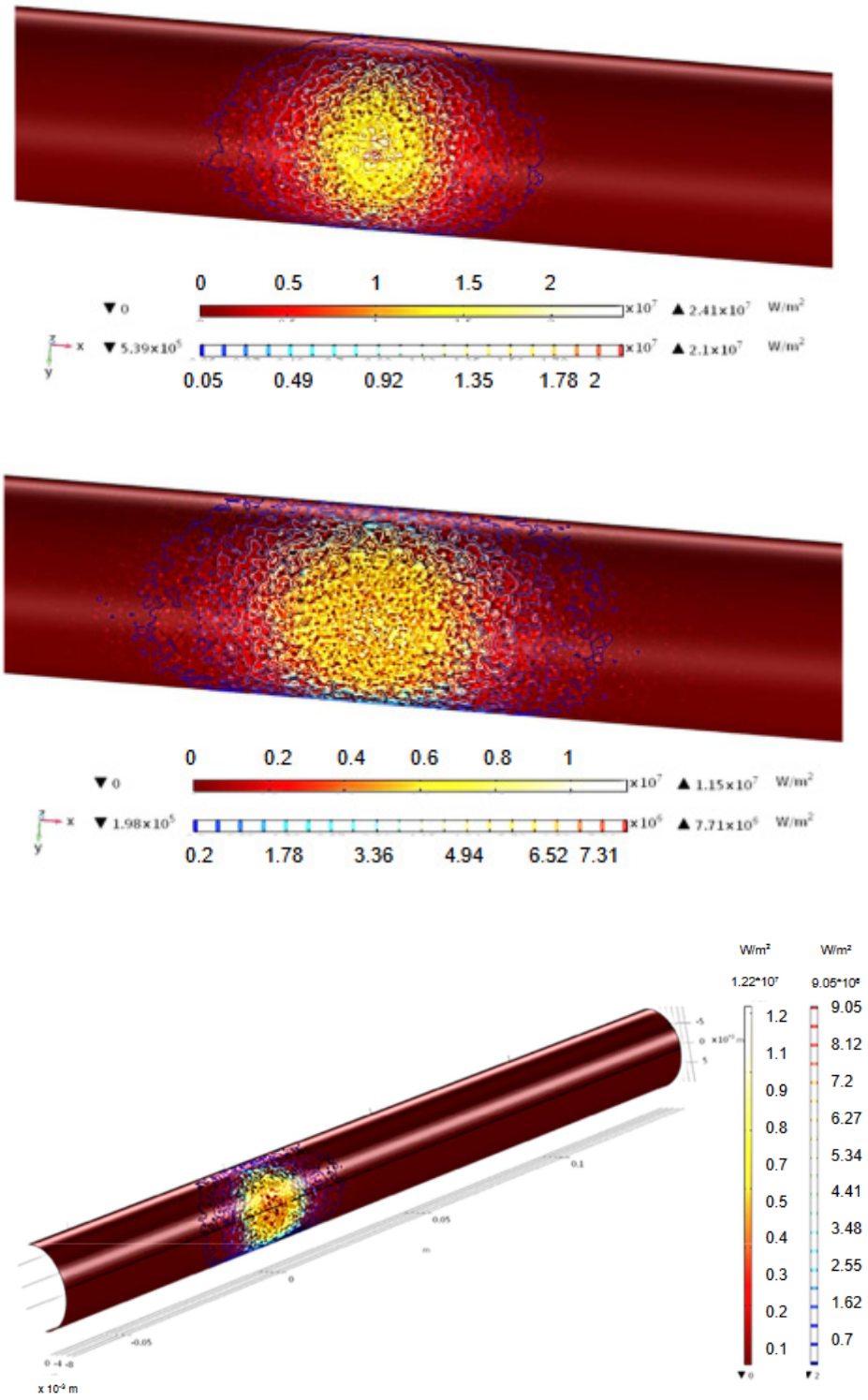

Figure 13. Three-dimensional distribution of thermal power deposited in the central section of receiver. Ideal case (**above**) or real case: perfectly smooth and reflective parabolic reflector; the phenomenon of solar limb darkening was neglected. Real case (**below**): parabolic reflector in which factors such as surface roughness, absorption and solar limb darkening were included.

Table 1. Geometrical and physical parameters used in the study and scheme of the multiphysical model.

Modeling procedure in Comsol Multiphysics			
MODEL CREATION:			
Selection of the model geometry → 3D geometry			
Selection of physics → optics > ray optics > geometrical optics (GOP).			
Study definition → ray-tracing simulation			
GEOMETRICAL AND PHYSICAL PARAMETERS [44]:			
Name	**Expression**	**Value**	**Description**
f	0.92 (m)	0.92 m	Focal length
Phi	45 (deg)	0.7854 rad	Rim angle
D	4 × f × (csc(phi)-cot(phi))	1.80 m	Dish diameter
A	Pi × d^2/4	2.544 m^2	Dish projected surface area
Psim	4.65 (mrad)	0.00465 rad	Maximum solar-disc angle
Sig	1.75 (mrad)	0.00175 rad	Surface slope error
I_0	0.8 (kW/m^2)	800 W/m^2	Solar irradiance
GEOMETRY AND CREATION OF THE MESH:			
Receiver → horizontal cylinder			
Solar dish → Ray Optics Module > 3D > mirrors > Paraboloidal Reflector Shell 3D			
GEOMETRICAL OPTICS (GOP):			
Illuminated Surface 1 → ideal reflector ($\alpha = 0$)			
Illuminated Surface 2 → real reflector ($\alpha = 0.2$)			
Wall I → focal plane			
Deposited ray power → incident thermal flux on the focal plane (W/m^2)			

The temperature distribution in the focal plane reflected the thermal flow exactly. An analysis of the two-dimensional and three-dimensional temperature maps for the central section of the receiver was carried out, and is shown in Figure 14, to better understand the thermal response of the component exposed to the beam of solar radiation reflected by the concentrator. As for the evaluation of the deposited flow, also in this case, two different Monte Carlo ray-tracing simulations were performed, keeping the geometry and the radiation power intensity (equal to I_0) unchanged, see Table 2. The properties related to the parabolic mirror were instead modified. From the simulation executed considering the ideal parabolic reflector, an extremely high peak temperature was achieved, equal to about 4500 K, and the incident rays appeared slightly scattered with respect to the center of the focal plane, thanks to the perfect paraboloid reflectivity. The result was a homogeneous distribution characterized by an almost circular shape.

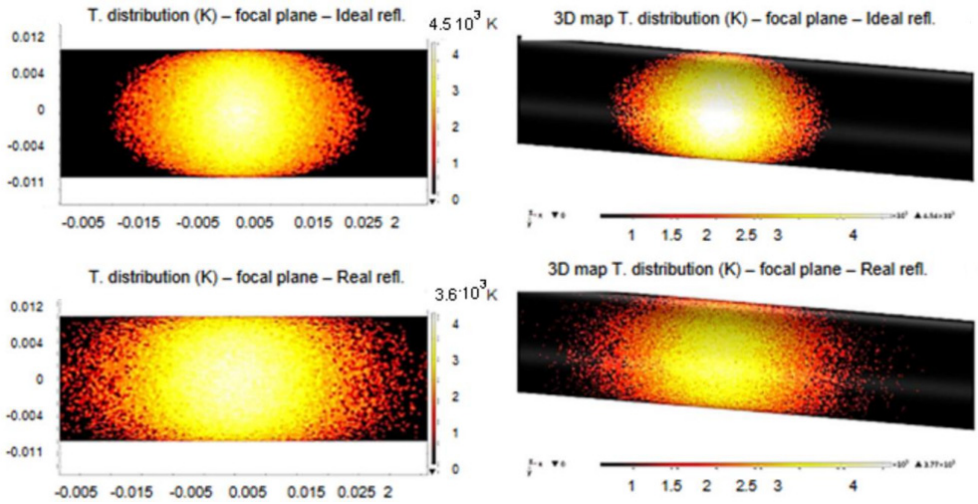

Figure 14. Two-/three-dimensional temperature distribution in the focal plane of the receiver. Ideal case (**above**): perfectly smooth and reflective parabolic reflector; the phenomenon of solar limb darkening was neglected. Real case (**below**): parabolic reflector in which factors such as surface roughness, absorption and solar limb darkening were included.

Table 2. Maximum thermal flow values deposited in focal plane of receiver and relative maximum power in target assessed assuming area of concentration with radius equal to 1 cm.

Case	Maximum Thermal Flux Deposited in Focal Plane (W/m^2)	Target Surface (m^2)	Maximum Power in Target (kW)
Ideal	$2.41 \ldots 10^7$	$3.141 \ldots 10^{-4}$ (r = 1 cm)	7.57
Real	$1.15 \ldots 10^7$		3.61

On the contrary, it was evident that for a real concentrator, no longer perfectly reflective and influenced by the limb-darkening phenomenon, the temperature distribution in the focal plane was more heterogeneous and characterized by significant dispersion. The attenuation of power due to the limb-darkening effect followed an approach similar to that studied and investigated by Lee et al. [46] using the relations reported by Buie et al. [47]. The maximum temperature in the center of the concentration surface approached 3600 K.

The ray-tracing simulations made it possible to evaluate the main parameters in a very limited area of the receiver, corresponding precisely to the focal plane located in the center section of the component. The treatment performed so far excluded many effects that generally tend to further reduce the flux and temperature values in the focal plane. It was, therefore, essential to implement additional modeling that focused on a more realistic study of the thermal field in the receiver. The main goal of the manuscript was to predict the overall temperature range of the receiver. This result could be used to assess which materials are the most suitable to be used for cables, thermocouples and fittings (Teflon or brass). To create a more realistic two-dimensional modeling, allowing a complete view of the temperature distribution over the entire surface of the receiver to be obtained, the procedure adopted followed the following steps:

(a) Evaluation of the average heat flux and the average temperature in the focal plane starting from the 2D distributions obtained through ray-tracing simulations carried out considering the real reflector (Figure 12/Figure 14). The data exported from Comsol were imported into Matlab for processing;
(b) Two-dimensional geometric modeling of the receiver with a concentration surface having a circular shape;
(c) Simulation of a stationary study by entering the following conditions:
    - Initial receiver temperature: Ambient = 293.15 K;
    - Imposition of the average and constant heat flux calculated in point (a) for the entire concentration area mentioned in (b). The heat source imposed in the focal zone of the receiver was measured as $P_{imposed} = \phi_{Avg} \cdot A_{foc}$;
    - Convective heat flow from the external edges of the receiver (convection with external air).

The results thus obtained (Figure 15) provided a maximum temperature in the focal plane, with an ideal solar radiation I_0, equal to about 1800 °C, the same temperature declared by the manufacturer for the concentrator operating under the maximum available solar irradiation [44]. The ray-tracing simulation model created with Comsol was "idealized", which is why the temperature values obtained in Figure 14 showed high values. Convection with outside air and the resulting heat dissipation with the surroundings caused a significant reduction in temperature compared with the ideal case.

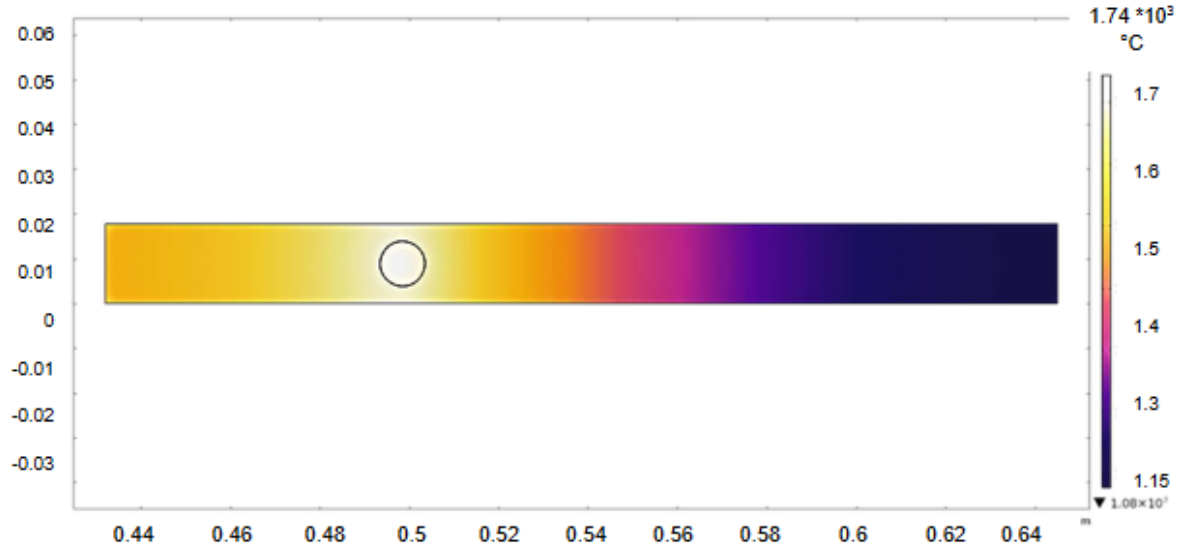

Figure 15. Two-dimensional temperature map for horizontal cylindrical receiver considering the actual exposure of the component to external atmosphere and consequent heat dissipation via convection (steady-state conditions).

3.3. Theoretical Temperature Forecast for Future Development

Unlike the ideal case, in which the continuous operation of the system exposed to maximum incident solar irradiance was hypothesized, in a real situation, it is necessary to analyze the behavior encountered by the system when forced to operate with variable irradiation both during the day and with the changing seasons. For this reason, an additional simulation concerning the real case was implemented to provide a useful forecasting model that would allow us to make a realistic estimate of the producibility of the system for the different periods of the year. Such a solution appeared reasonable given the perennial repetition of the seasons that, unless sudden and unpredictable changes in the temperature happen due to climate change, punctually and cyclically show similar global trends in radiation and maximum or minimum temperature depending on the location considered. The irradiance values were detected using a solarimeter (pyrheliometer/pyranometer) located in Turin (Energy Center). By comparing the same periods belonging to different solar years, it was clear how each month is subject to a completely random rate of variation in climatic conditions.

For this reason, it is not appropriate to assess global radiation trends, both monthly and seasonal ones, from the overall average of solar radiation data. The most reasonable procedure is, therefore, to produce a comparison of global radiation trends for the different meteorological seasons of the year. For each curve, the precise radiation values corresponding to the individual time instants were the result of the averaging of the values for the central day of each month in the case of a clear, sunny day. Alternatively, we had to switch to adjacent days until we found the data of the day that offered the best values, in terms of limiting the random effects of cloudiness and precipitation. Once the reference days for the various months of the year were found, the average of the three values was calculated, thus obtaining the seasonal distributions of global radiation, as illustrated in Figure 16. As can be seen, the outermost curves, especially the summer curve, offered considerable radiation values over a much longer period than the other seasons. Being able to expose the solar disc to such high values of radiative intensity would result in a higher yield in the warmer months, due to the higher amount of energy absorbed by the concentrator, thus making the entire analyzed technology very interesting.

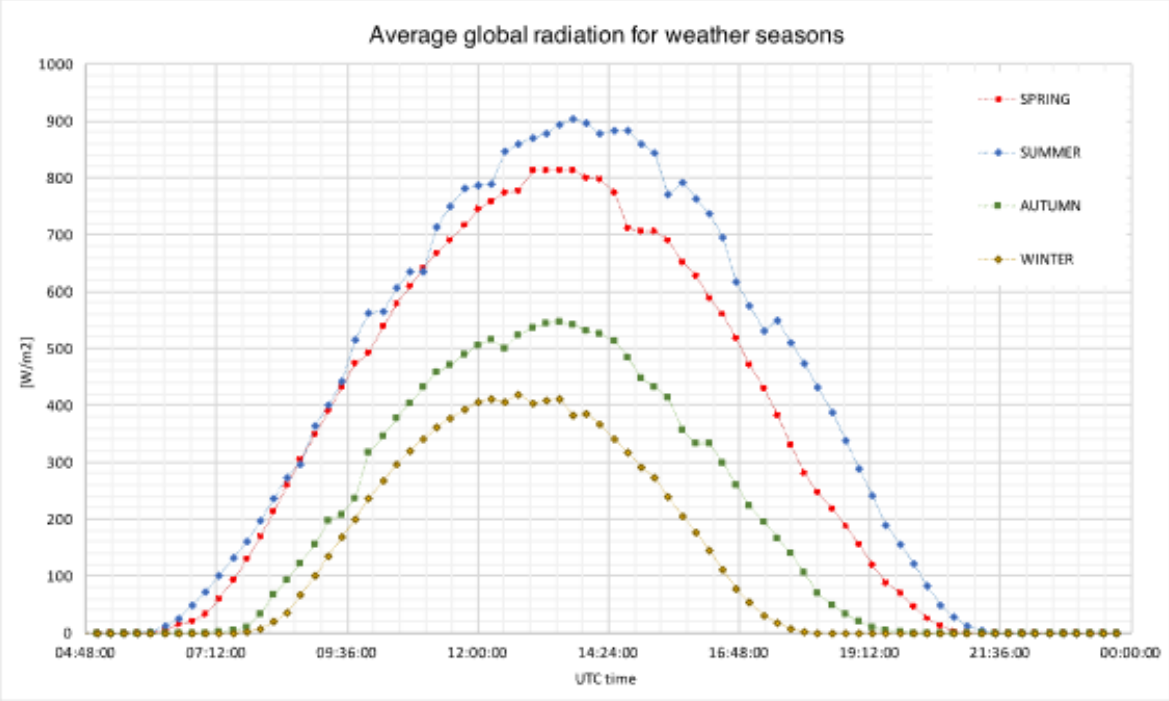

Figure 16. Trend of average global radiation during the day for different weather seasons. The time values were obtained as averages of radiation values for the clearest and sunniest days of each month.

At this point, the corresponding temperature distribution in the vicinity of the reactor was determined over time. Since the research study began in October, it was possible to validate the model for the winter season, since the experimental information was measured using the thermocouples positioned in the receiver. In the case of the summer months, on the other hand, as only global radiation data were available for the months of 2019–2021, the reactor temperature values were obtained mathematically using the specially designed 2D model of the dish and solar receiver. In the table below (Table 3), the list of data with the uncertainty values is presented.

Table 3. Average global radiation registered at the POLITO weather station.

	2019		2020		2021	
2019–2021	**Global Radiation (W/m^2)**	**Uncertainty (W/m^2)**	**Global Radiation (W/m^2)**	**Uncertainty (W/m^2)**	**Global Radiation (W/m^2)**	**Uncertainty (W/m^2)**
Summer	430.0	28.1	430.1	28.2	411.7	15.1
Autumn	191.3	14.0	226.6	14.3	228.4	12.0
Winter	115.0	18.1	213.9	17.3	196.6	17.0
Spring	209.3	28.2	314.8	28.5	327.2	10.7

A structured forecast model was used to simulate the actual behavior of the system subject to the inevitable seasonal cyclicality. The aim was to estimate the main process parameters found in the warmest and sunniest months, during which the irradiation values were close to ideal. In this case, a solar thermochemical reactor would operate under optimal production conditions, guaranteeing the maximum yield of chemical compounds according to the tested process. The receiver temperature profile is reported below. These values were obtained using the simulation and modeling approach in spring and in summer and were compared with actual values taken as reference on specific days in the winter period (see Table 4).

Table 4. Average temperature values in the middle of the receiver.

	12/12—13:00		11/1—13:00		22/1—13:00	
Temperature (°C)	Model	Experimental	Model	Experimental	Model	Experimental
	455	442.8	466	461.3	478	472.5

The reactor temperature was then derived from the seasonal average values of variable irradiance, which was appropriately imported into Comsol to perform a simulation of the entire system using the parametric sweep function for the entire year. The data correlated with the 2D heat flux maps were subsequently exported and processed in Matlab to obtain the average heat-flux and temperature values in the focal plane, which in turn were used in a simplified 2D model. It should be noted that the 3D model did not consider all those effects that further reduce the temperature in the focal plane of the receiver, such as conduction and convection with the external environment, which were instead integrated in the 2D model. The reactor temperatures corresponding to each average radiation value are, therefore, shown in Figure 17. As reported in the study by Bekele et al., the importance of irradiance intensity was shown for the receiver temperature increase [22]. A cylindrical receiver was studied, achieving a heat flux of 32.4 MW/m^2 and a temperature of 923 K.

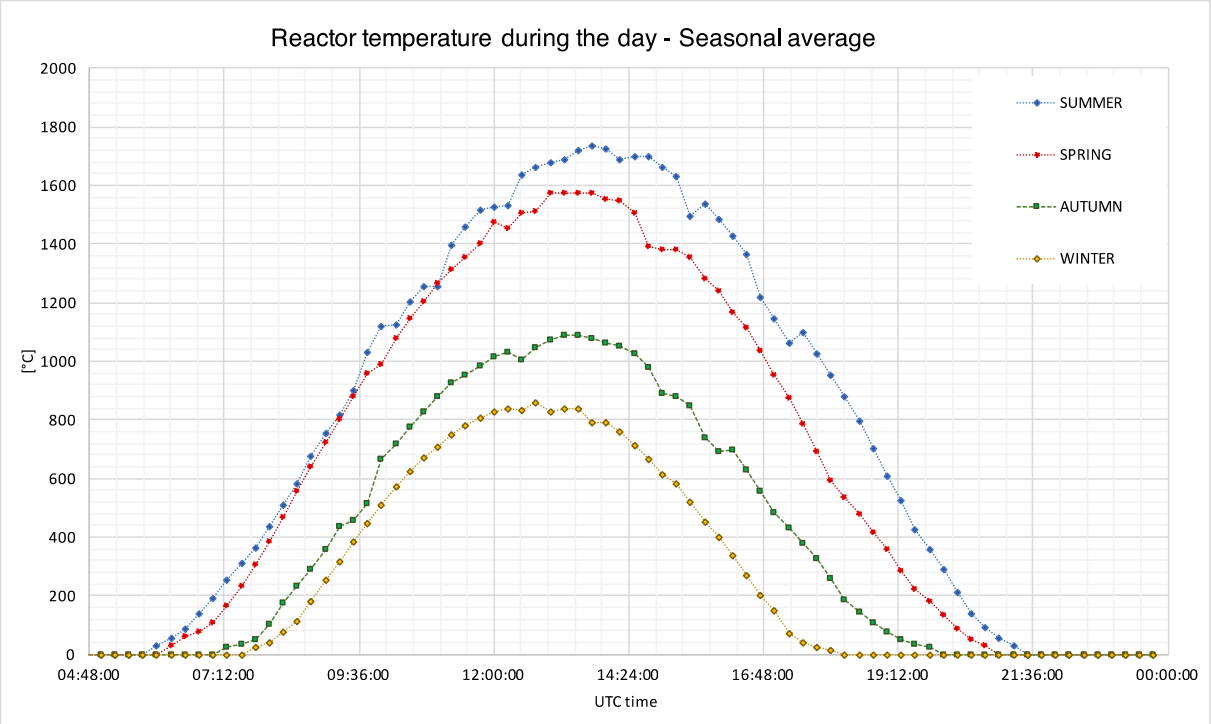

Figure 17. Reactor temperature during the day for different weather seasons. The time values were obtained as a result of the 2D model developed in Comsol Multiphysics.

4. Conclusions

The work conducted aimed to address and to study the performance of a solar-concentrator prototype. Experimental temperatures monitored inside a ceramic receiver during the operation of a solar concentrator were used. The solar concentrator was installed on the roof of the Energy Centre, and it was used to study the reduction and oxidation reactions of metal oxides. The study focused on a typical year by identifying the best times to reach temperatures above 1000 °C to be able to reduce metal oxides even under methane-assisted conditions [51]. From the spring season until the end of the summer season, optimum conditions were reached for working experimentally with iron oxides and for carrying out thermochemical reactions, in particular the reduction reaction, which

takes place at high temperatures. The model proposed was experimentally validated in the winter season with the receiver temperature of the solar dish. The experimental results differed from the modeling results in a range of less than 5%. Finally, these results were used to trigger an experimental campaign on the reduction reaction with iron oxides. For the remainder of the time, i.e., in the autumn and winter seasons, the solar concentration system could be used for thermal energy storage purposes [52] or to feed a Stirling engine for electrical-energy production [53].

Author Contributions: Conceptualization, E.M. and D.P.; methodology, E.M. and D.P.; software, E.M.; validation, D.P.; investigation, E.M. and D.P.; resources, D.P.; data curation, E.M.; writing—original draft preparation, D.P. and E.M.; writing—review and editing, D.P.; supervision, D.P. and M.S.; project administration, M.S.; funding acquisition, M.S. All authors have read and agreed to the published version of the manuscript.

Funding: This research received external funding from INFRA-P, Piemonte. POR-FESR 2014–2020. The APC was funded by [D.P.].

Informed Consent Statement: Informed consent was obtained from all subjects involved in the study.

Acknowledgments: Information on funds received: The prototype test bench was partially financed by the regional INFRA-P call of the Piedmont region.

Conflicts of Interest: The authors declare no conflict of interest.

Nomenclature List

A_0	Frontal area of parabolic mirror
A_{foc}	Focal area (m^2)
BEM	Boundary Element Method
CDS	Carbon-dioxide splitting
CS	Concentrating solar system
CSP	Concentrated solar power
CSR	Circumsolar relationship
CTL	Coal-To-Liquid (CTL)
D_{dish}	Dish diameter (m)
f	Focal length
FEM	Finite element method
GTL	Gas-To-Liquid (GTL)
I_0	Ideal solar irradiance (800 W/m^2)
I_t	Intensity threshold of reflected rays (10^{-3} W/m^2)
n_i	Refractive index of i-th material
$P_{imposed}$	Power imposed (kW)
P_{th}	Radiative power concentrated in the reaction zone (kW)
P_{source}	Power of the source (kW)
Psim	Maximum solar disc angle (mrad)
Sig	Surface slope error (mrad)
WS	Water splitting
α,	Absorption coefficient of mirror
θ_i	Angle between i-th incident ray and surface normal
θ_s	Maximum opening angle of the solar disk (4.65 mrad)
ϕ_{Avg}	Average specific thermal flux (kW/m^2)
ψ	Rim angle

References

1. Agrafiotis, C.; Roeb, M.; Sattler, C. A review on solar thermal syngas production via redox pair-based water/carbon dioxide splitting thermochemical cycles. *Renew. Sustain. Energy Rev.* **2015**, *42*, 254–285. [CrossRef]
2. Wood, D.; Nwaoha, C.; Towler, B. Gas-to-liquids (GTL): A review of an industry offering several routes for monetizing natural gas. *J. Nat. Gas Sci. Eng.* **2012**, *9*, 196–208. [CrossRef]

3. Karakaya, C.; Kee, R.J. Progress in the direct catalytic conversion of methane to fuels and chemicals. *Prog. Energy Combust. Sci.* **2016**, *55*, 60–97. [CrossRef]
4. Spivey, J.J. *Catalysis: Volume 9*; Royal Society of Chemistry: London, UK, 2007.
5. Sosna, M.K.; Goltibeva, I.A.; Kononenko, A.A.; Zaichenko, V.A.; Grishina, I.N.; Korolev, E.V. Prospects of Base Oil Production by GTL Technology in Russia. *Chem. Technol. Fuels Oils* **2019**, *54*, 751–758. [CrossRef]
6. Gupta, P.K.; Kumar, V.; Maity, S. Renewable fuels from different carbonaceous feedstocks: A sustainable route through Fischer–Tropsch synthesis. *J. Chem. Technol. Biotechnol.* **2020**, *96*, 853–868. [CrossRef]
7. Bayon, A.; de la Calle, A.; Ghose, K.K.; Page, A.; McNaughton, R. Experimental, computational and thermodynamic studies in perovskites metal oxides for thermochemical fuel production: A review. *Int. J. Hydrogen Energy* **2020**, *45*, 12653–12679. [CrossRef]
8. Giaconia, A.; Caputo, G.; Turchetti, L.; Monteleone, G. *A New Generation of Renewable Powered Reforming Processes, Energia, Ambiente e Innovazione*; URL to the ENEA Report; Rome, Italy, 2021; Available online: https://www.eai.enea.it/?option=com_content&view=article&id=1242&Itemid=1719 (accessed on 27 July 2022). [CrossRef]
9. Agrafiotis, C.; von Storch, H.; Roeb, M.; Sattler, C. Solar thermal reforming of methane feedstocks for hydrogen and syngas production—A review. *Renew. Sustain. Energy Rev.* **2014**, *29*, 656–682. [CrossRef]
10. Ngoh, S.K.; Njomo, D. An overview of hydrogen gas production from solar energy. *Renew. Sustain. Energy Rev.* **2012**, *16*, 6782–6792. [CrossRef]
11. Zhang, Y.; Xu, C.; Chen, J.; Zhang, X.; Wang, Z.; Zhou, J.; Cen, K. A novel photo-thermochemical cycle for the dissociation of CO_2 using solar energy. *Appl. Energy* **2015**, *156*, 223–229. [CrossRef]
12. Fresno, F.; Fernández-Saavedra, R.; Gómez-Mancebo, M.B.; Vidal, A.; Sánchez, M.; Rucandio, I.; Quejido, A.J.; Romero, M. Solar hydrogen production by two-step thermochemical cycles: Evaluation of the activity of commercial ferrites. *Int. J. Hydrogen Energy* **2009**, *34*, 2918–2924. [CrossRef]
13. Smestad, G.P.; Steinfeld, A. Review: Photochemical and Thermochemical Production of Solar Fuels from H_2O and CO_2 Using Metal Oxide Catalysts. *Ind. Eng. Chem. Res.* **2012**, *51*, 11828–11840. [CrossRef]
14. Fang, J.; Wu, H.; Liu, T.; Zheng, Z.; Lei, J.; Liu, Q.; Jin, H. Thermodynamic evaluation of a concentrated photochemical–photovoltaic–thermochemical (CP-PV-T) system in the full-spectrum solar energy utilization. *Appl. Energy* **2020**, *279*, 115778. [CrossRef]
15. Meier, A.; Steinfeld, A. Solar Energy in Thermochemical Processing. In *Solar Thermal Energy*; Alexopoulos, S., Kalogirou, S.A., Eds.; Springer: New York, NY, USA, 2022; pp. 315–347. [CrossRef]
16. Abanades, S.; Flamant, G. Thermochemical hydrogen production from a two-step solar-driven water-splitting cycle based on cerium oxides. *Sol. Energy* **2006**, *80*, 1611–1623. [CrossRef]
17. Abanades, S.; Villafan-Vidales, I. CO_2valorisation based on Fe_3O_4/FeO thermochemical redox reactions using concentrated solar energy: Solar thermochemical dissociation of CO_2. *Int. J. Energy Res.* **2012**, *37*, 598–608. [CrossRef]
18. Alenazey, F.; Alyousef, Y.; Almisned, O.; Almutairi, G.; Ghouse, M.; Montinaro, D.; Ghigliazza, F. Production of synthesis gas (H2 and CO) by high-temperature Co-electrolysis of H2O and CO2. *Int. J. Hydrogen Energy* **2015**, *40*, 10274–10280. [CrossRef]
19. Küngas, R. Review—Electrochemical CO_2 Reduction for CO Production: Comparison of Low- and High-Temperature Electrolysis Technologies. *J. Electrochem. Soc.* **2020**, *167*, 044508. [CrossRef]
20. De Falco, M.; Piemonte, V. Solar enriched methane production by steam reforming process: Reactor design. *Int. J. Hydrogen Energy* **2011**, *36*, 7759–7762. [CrossRef]
21. Ho, C.K. Advances in central receivers for concentrating solar applications. *Sol. Energy* **2017**, *152*, 38–56. [CrossRef]
22. Bekele, E.A.; Ancha, V.R.; Binchebo, T.L. Analysis of Solar Irradiance Variation on Heat Flux and Temperature Distribution for a Dish Concentrator Receiver. *ASME Open J. Eng.* **2022**, *1*, 11011. [CrossRef]
23. Wang, M.; Siddiqui, K. The impact of geometrical parameters on the thermal performance of a solar receiver of dish-type concentrated solar energy system. *Renew. Energy* **2010**, *35*, 2501–2513. [CrossRef]
24. Burgaleta, J.I.; Arias, S.; Ramirez, D. Gemasolar, the first tower thermosolar commercial plant with molten salt storage. In Proceedings of the 17th SolarPACES Conference, Granada, Spain, 20–23 September 2011.
25. Hering, W.; Stieglitz, R.; Wetzel, T. Application of liquid metals for solar energy systems. *EPJ Web Conf.* **2012**, *33*, 03003. [CrossRef]
26. Agrafiotis, C.; von Storch, H.; Roeb, M.; Sattler, C.; Hydrogen production by solar thermal methane reforming. Chapter 23 of Transition to Renewable Energy Systems. *Wiley-VCH Verlag GmbH & Co. KGaA*. Available online: https://onlinelibrary.wiley.com/doi/abs/10.1002/9783527673872.ch23 (accessed on 27 July 2022). [CrossRef]
27. Chuayboon, S.; Abanades, S. An overview of solar decarbonization processes, reacting oxide materials, and thermochemical reactors for hydrogen and syngas production. *Int. J. Hydrogen Energy* **2020**, *45*, 25783–25810. [CrossRef]
28. Rathod, V.P.; Shete, J.; Bhale, P.V. Experimental investigation on biogas reforming to hydrogen rich syngas production using solar energy. *Int. J. Hydrogen Energy* **2015**, *41*, 132–138. [CrossRef]
29. Scheffler, M.; Colombo, P. *Cellular Ceramics: Structure, Manufacturing, Properties and Applications*; John Wiley & Sons: Hoboken, NJ, USA, 2006.
30. Berman, A.; Karn, R.K.; Epstein, M. Steam reforming of methane on a Ru/Al2O3 catalyst promoted with Mn oxides for solar hydrogen production. *Green Chem.* **2007**, *9*, 626–631. [CrossRef]
31. Klein, H.H.; Karni, J.; Rubin, R. Dry Methane Reforming Without a Metal Catalyst in a Directly Irradiated Solar Particle Reactor. *J. Sol. Energy Eng.* **2009**, *131*, 021001. [CrossRef]

32. Karni, J.; Kribus, A.; Doron, P.; Rubin, R.; Fiterman, A.; Sagie, D. The DIAPR: A High-Pressure, High-Temperature Solar Receiver. *J. Sol. Energy Eng.* **1997**, *119*, 74–78. [CrossRef]
33. Hosseini, F.; Siavashi, M. Optimization of SMR process for syngas production through a solar-assisted thermo-chemical reactor with a multi-layered porous core. *Sol. Energy* **2021**, *230*, 208–221. [CrossRef]
34. Yaashikaa, P.R.; Kumar, P.S.; Varjani, S.J.; Saravanan, A. A review on photochemical, biochemical and electrochemical transformation of CO2 into value-added products. *J. CO_2 Util.* **2019**, *33*, 131–147. [CrossRef]
35. Foit, S.R.; Vinke, I.C.; de Haart, L.G.J.; Eichel, R.-A. Power-to-Syngas: An Enabling Technology for the Transition of the Energy System? *Angew. Chem. Int. Ed.* **2017**, *56*, 5402–5411. [CrossRef]
36. Hernández, S.; Farkhondehfal, M.A.; Sastre, F.; Makkee, M.; Saracco, G.; Russo, N. Syngas production from electrochemical reduction of CO_2: Current status and prospective implementation. *Green Chem.* **2017**, *19*, 2326–2346. [CrossRef]
37. Lu, Y.; Zhu, L.; Agrafiotis, C.; Vieten, J.; Roeb, M.; Sattler, C. Solar fuels production: Two-step thermochemical cycles with cerium-based oxides. *Prog. Energy Combust. Sci.* **2019**, *75*, 100785. [CrossRef]
38. Cabeza, L.F.; Solé, A.; Fontanet, X.; Barreneche, C.; Jové, A.; Gallas, M.; Prieto, C.; Fernández, A.I. Thermochemical energy storage by consecutive reactions for higher efficient concentrated solar power plants (CSP): Proof of concept. *Appl. Energy* **2017**, *185*, 836–845. [CrossRef]
39. Pan, H.; Li, Y.; Zhu, L.; Lu, Y. Solar-driven H2O/CO2 conversion to fuels via two-step electro-thermochemical cycle in a solid oxide electrochemical cell. *Energy Convers. Manag.* **2022**, *259*, 115578. [CrossRef]
40. Wang, B.; Li, X.; Dai, Y.; Wang, C.-H. Thermodynamic analysis of an epitrochoidal rotary reactor for solar hydrogen production via a water-splitting thermochemical cycle using nonstoichiometric ceria. *Energy Convers. Manag.* **2022**, *268*, 115968. [CrossRef]
41. Sami, A.; Mehrpooya, M.; Noorpoor, A. Investigation of an integrated thermochemical hydrogen production and high temperature solar thermochemical energy storage and CO_2 capture process. *Appl. Therm. Eng.* **2022**, *214*, 118820. [CrossRef]
42. Shahabuddin, M.; Alim, M.; Alam, T.; Mofijur, M.; Ahmed, S.; Perkins, G. A critical review on the development and challenges of concentrated solar power technologies. *Sustain. Energy Technol. Assessments* **2021**, *47*, 101434. [CrossRef]
43. How to Model Solar Concentrators with the Ray Optics Module, COMSOL. (n.d.). Available online: https://www.comsol.it/blogs/how-to-model-solar-concentrators-with-the-ray-optics-module/ (accessed on 20 June 2022).
44. *Manuale Uso e Manutenzione—Concentratore Solare a Disco*; Luminari, L. (Ed.) Technical Data Sheet; ELMA Srl: Riva del Garda, TN, Italy, 2019.
45. Colombo, L. *Studio Parametrico Delle Prestazioni Energetiche di Collettori Solari con Concentratori Parabolici Composti (CPC) Nella Produzione di Calore a Media Temperature*; Politecnico di Milano: Milan, Italy, 2012.
46. Lee, H. The geometric-optics relation between surface slope error and reflected ray error in solar concentrators. *Sol. Energy* **2014**, *101*, 299–307. [CrossRef]
47. Buie, D.; Monger, A.; Dey, C. Sunshape distributions for terrestrial solar simulations. *Sol. Energy* **2003**, *74*, 113–122. [CrossRef]
48. Alqurashi, M.M.; Ganash, E.A.; Altuwirqi, R.M. Simulation of a Low Concentrator Photovoltaic System Using COMSOL. *Appl. Sci.* **2022**, *12*, 3450. [CrossRef]
49. Ubando, A.T.; Conversion, A.; Barroca, R.B.; Enano, N.H.; Espina, R.U. Computational Fluid Dynamics on Solar Dish in a Concentrated Solar Power: A Bibliometric Review. *Solar* **2022**, *2*, 251–273. [CrossRef]
50. Baig, H.; Sarmah, N.; Heasman, K.C.; Mallick, T.K. Numerical modelling and experimental validation of a low concentrating photovoltaic system. *Sol. Energy Mater. Sol. Cells* **2013**, *113*, 201–219. [CrossRef]
51. Zayed, M.E.; Zhao, J.; Elsheikh, A.H.; Li, W.; Sadek, S.; Aboelmaaref, M.M. A comprehensive review on Dish/Stirling concentrated solar power systems: Design, optical and geometrical analyses, thermal performance assessment, and applications. *J. Clean. Prod.* **2020**, *283*, 124664. [CrossRef]
52. Triscari, G.; Santovito, M.; Bressan, M.; Papurello, D. Experimental and model validation of a phase change material heat exchanger integrated into a real building. *Int. J. Energy Res.* **2021**, *45*, 18222–18236. [CrossRef]
53. Papurello, D.; Bertino, D.; Santarelli, M. CFD Performance Analysis of a Dish-Stirling System for Microgeneration. *Processes* **2021**, *9*, 1142. [CrossRef]